Unravelling the collagen network of the arterial wall

Beenakker, J.W.M.

3 Methods

In this thesis several different biological imaging techniques are used to image various collagen containing samples and to measure their mechanical properties. Table 3.1 shows an overview of the techniques used in this study with their specific features and characteristics.

In this chapter we will discuss AFM and fluorescence microscopy in relation to our experiments on collagen.

3.1 Atomic Force Microscopy

The Atomic Force Microscope[1] (AFM), a member of the more general class of Scanning Probe Microscopes, has become a valuable tool for biologists, physicists and chemists to perform a various number of measurements on the nano-scale. Since their invention in 1982 by Binnig and Rohrer,[2] Scanning Probe Microscopes have changed the modern natural sciences by contributing to major progress in the understanding of the structure and properties of condensed matter. The many different measurement techniques of the AFM and its ability to operate under aqueous conditions have made the AFM a popular tool in most of the natural sciences. The AFM has been used for high resolution imaging of material surfaces including, metals[3] and polymers,[4] but also of biological systems like DNA,[5, 6] proteins[7–9] and whole cells.[10, 11] Other applications of the AFM include nano manipulation,[12] friction measurements,[13] protein mapping[14, 15] and MRI imaging.[16] In this study the AFM is mainly used as a tool to perform nano-indentations.

3.1.1 The Atomic Force Microscope

The unique resolution of the AFM is based on an ultra-sharp tip, with a typical radius of 20 nm, which is attached to a flexible cantilever (fig. 3.1a). The cantilever is accurately moved with respect to the sample in x, y and z by ceramic piezoelements, which allow the sample to be scanned with sub-nanometer resolution while maintaining a constant force between the sample and the AFM tip (fig. 3.1b). The force between sample and tip is commonly determined by deflecting a laser beam of the end of the cantilever and measuring its deflection with a four-quadrant photodiode. Tip-sample interactions include electrostatic repulsion, van der Waals attraction, capillary and frictional forces.

The AFM used in this study, a Molecular Imaging Picoscan AFM, is mounted on a Zeiss Axiovert inverted microscope to allow for a precise selection of the scanned area, as is depicted in fig. 3.1c. The whole setup is put in an acoustic box to reduce acoustic and electronic noise on the one hand and to minimize the thermal drift on the other. A custom built heating and cooling system allows

Microscopy	Resolution limit	Specific features and characteristics
Light microscopy	~ 0.2 µm	Samples can be imaged in liquid or air. The resolution is limited by the wavelength of visible light.
Fluorescence microscopy	~ 0.2 µm	Samples can be imaged in liquid or air. Fluorescent labels are used to localize molecular components within the sample. Confocal microscopy further enables three-dimensional studies of the sample.
Scanning electron microscopy (SEM)	~ 5 nm	The sample placed is in a vacuum and is often coated, as the technique generally requires an electron conductive surface. An electron beam is used to probe the surface of the sample. Specific surface molecules can be labeled with heavy metals.
Atomic force microscopy (AFM)	~ 5 nm ~ 100 pN	Samples can be imaged in liquid or air. Imaging is accomplished by monitoring the position of a sharp tip, attached to a micro-cantilever, while it is scanned over the sample surface. The AFM provides a three-dimensional visualization of the sample surface and can also be used to measure the mechanical properties of the sample.

Table 3.1: Overview of characteristics of the main microscopy tools used in this study.

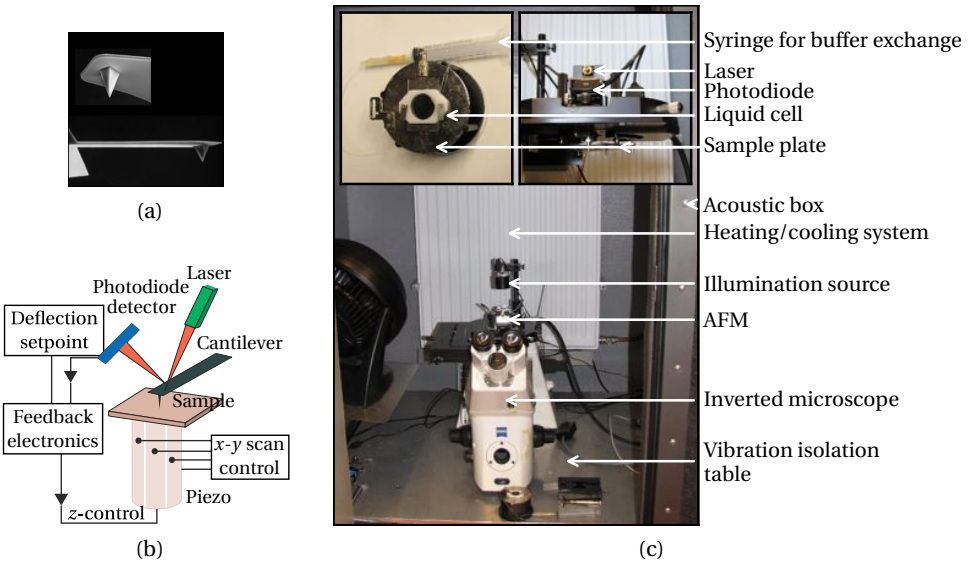

Figure 3.1:
(a) SEM image of an AFM cantilever (± 100 µm long) and an AFM tip (20 nm radius).
(b) Schematic representation of an AFM. A cantilever with a very sharp tip scans the sample, while the feedback electronics maintain a constant deflection of the cantilever.[17]
(c) The AFM, mounted on an inverted microscope, is put in an acoustic box to reduce the noise and thermal drift. A heating system is installed to control the temperature in the box.

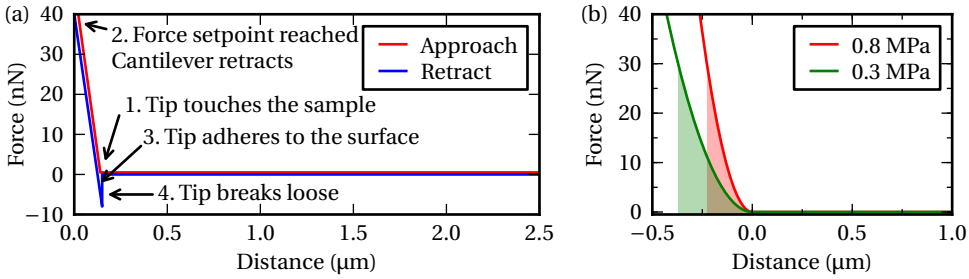

Figure 3.2:
(a) A typical force-distance curve made on glass. The cantilever approaches the surface until the force setpoint, 40 nN, is reached and retracts.
(b) Force-distance curves made on a stiff and a soft substrate by a conical indenter. The relative stiffness of the samples can be obtained by comparing the work needed to reach the same repulsive force (30 nN).

the temperature in the box to be set. A small fluid cell, clamped on the sample, facilitates measurements in aqueous conditions.

The AFM has been equipped with a break-out box, which gives access to the individual signals sent between the AFM scanner and its electronics. By sampling the deflection signal with a National Instruments acquisition card and controlling the AFM with a custom scripting program written in LabVIEW and Visual Basic 6, nano-indentation measurements are made with an enhanced resolution of approximately ten thousand points per indentation instead of a few hundred points.

3.1.2 Nano-indentation measurements

The AFM's ability to measure small forces, has made it a valuable instrument to measure the local mechanical properties of a wide range of samples.[18–21] By indenting the surface with the tip and measuring the force as a function of tip-sample distance, fig. 3.2, quantities such as sample stiffness, electrostatic interactions and adhesion forces can be measured.[17, 22–25]

In 1882, Heinrich Hertz modeled the indentation of a homogeneous sample with a spherical indenter.[26] This model, extended by Ian Sneddon for rotational symmetric indenters,[27] is commonly used to determine the Young's modulus, a measure of the sample stiffness, from a force-distance curve. The AFM tips used in this study can be approximated as a cone or a sphere, resulting in the

following relation between the force, F, and indentation, δ,

$$F_{cone} = \frac{\pi}{2}\frac{\tan(\alpha)E}{1-\nu}\delta^2 \tag{3.1}$$

$$F_{sphere} = \frac{4}{3}\frac{E\sqrt{R}}{1-\nu}\delta^{\frac{3}{2}}, \tag{3.2}$$

with E the Young's modulus and ν the Poisson ratio of the sample, α the opening angle of the cone and R the radius of the sphere.

A precise determination of the point of contact is necessary to apply the Hertz model to a force-distance curve. A small error in the determination of the point of contact due to the presence of a background signal and noise, often leads to a large error in the calculated stiffness. For rough and soft samples it can be difficult to control these errors, since forces at the moment of contact are often too small to give a measurable increase in the deflection signal. Optical distortions in tip-scanning AFM's tend to make these errors even larger (section 3.1.3). A-Hassan et al. developed a method, called FIEL (force integration to equal limits), to calculate the Young's modulus from a force-distance curve without the necessity to know the point of contact.[28]

By integrating the force, F, until a certain deformation, δ, the work needed for this deformation, W, is calculated: $W = \int_0^\delta F(z)dz$. This measure is directly related to the stiffness of the sample, as is illustrated in fig. 3.2b. Because the tip only starts to deflect when it indents the surface, there is no work performed until the point of contact. This allows the whole force-distance curve to be integrated, and removes the necessity to determine the point of contact. Rather, the problem is shifted to determining the zero of force. This error, however, is easier to control. By comparing the work needed with the work needed for the same deformation on a reference sample with a known stiffness, the stiffness of the sample can easily be calculated:

$$\frac{W_{sample}}{W_{calibration}} = \left(\frac{E_{calibration}}{E_{sample}}\right)^{\beta}, \tag{3.3}$$

with $\beta = \frac{1}{2}$ for a conical indenter and $\beta = \frac{3}{2}$ for a spherical indenter.

Ideally, this method of deriving the Young's modulus from a force-distance curve does not only remove the need to determine the point of contact, it also has several other advantages over fitting the Hertz model on the force-distance curve. Since the sensitivity of the system and the spring constant of the probe are the same in both measurements, they will divide out in equation 3.3, making it unnecessary to perform a calibration of the cantilever stiffness and to determine the optical lever sensitivity (which allows the bending of the cantilever to be

translated into the vertical deflection). This method is furthermore insensitive to small deviations in the tip geometry.

It proved, however, to be hard to produce a reference sample suitable to use as a comparison for measurements on the aortic wall. Various different types of reference samples with a stiffness similar to aortic tissue, 10^6 Pa,[29] have been tested, but they were either not stable over a longer period of time or were not suitable for AFM measurements, e.g. most synthetic polymers get sticky at low Young's moduli and thereby contaminate the cantilever. This calibration problem has been circumvented by modeling an indentation using equation 3.1 or 3.2. This method still allows for the whole force-distance curve to be integrated, but needs a precise calibration of the AFM setup and therefor lacks all the other advantages of the method proposed by A-Hassan et al. The spring constant, necessary to relate the cantilever deflection with the applied force, is calibrated with the Sader method[30] for rectangular cantilevers and with the thermal noise method[31–33] for triangular cantilevers.

The Hertz model describes the response of a homogenous and infinitely thick medium, whereas our samples have a finite thickness. By keeping the maximum indentation less than 10% of the sample thickness, the effect of supporting substrate turns out to be negligible.[34, 35] Hydrodynamic drag, caused by the surrounding buffer, could result in an extra loading force on the cantilever. The indentation rate is however chosen to be small enough, approximately 20 µm/s, to render the effects of hydrodynamic drag negligible.

The necessary condition of an isotropic, smooth substrate with a Young's modulus independent of the applied force, is however not met. Biological tissues tend to stiffen when they are deformed,[36, 37] and the many different types of fibers make the sample far from isotropic. However, by keeping the loading rate approximately constant amongst different experiments and using the same force-setpoint, the calculated values for the stiffness can still be used as a measure of the response of the tissue upon indentation. This "effective Young's modulus" will reflect the local mechanical properties of the tissue under the set experimental conditions and can be used to compare indentations on different types of tissue.

In this study we will indent the tissue on different equally spaced locations, e.g. a grid of 100 µm×100 µm containing 34 × 34 points. Such a measurement is often referred to as a force-volume measurement. By calculating the effective Young's modulus for every indentation a stiffness map of tissue is made, which can show local stiffness variations on the sub-micrometer level.

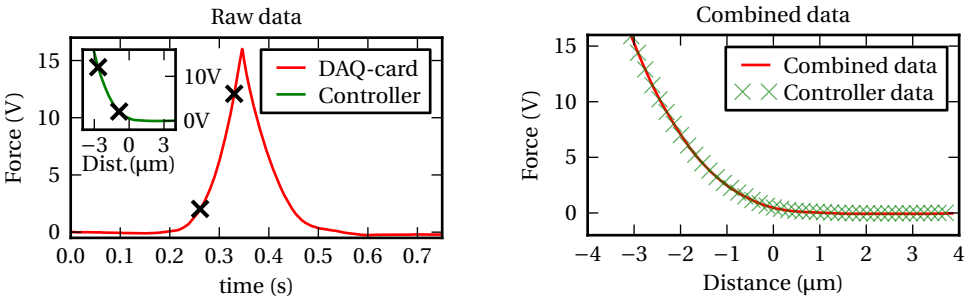

Figure 3.3:
Raw deflection data collected by the AFM controller and the DAQ-card. Two points, marked with an X, are used to correlate the DAQ-data to the data of the AFM controller and combine them into a force-distance curve with a higher resolution.

3.1.3 Data processing

Increase the time-resolution of indentation data

We use a National Instruments card controlled with a custom LabVIEW and Visual Basic script developed in the lab, to acquire force-distance curves with an enhanced time resolution. This resolution is needed because the increase of force can be very rapid and the AFM software only stores a limited number of data points per indentation. This enhancement is especially relevant for rough samples such as the human aorta, where the full piezo range in the z-direction is needed to indent the surface at different lateral positions.

The deflection versus time signal from the DAQ-card is transformed into a deflection versus piezo position dataset with a MATLAB script. This script determines the piezo position at two different indentation depths using the indentation data from the AFM-controller. By correlating these two indentation depths with the data from the DAQ-card, as is depicted in fig. 3.3, the piezo positions of the approach part of the force versus time data can be calculated by linear interpolation. Afterwards the χ^2 of the difference between the data from the AFM-controller and the high resolution force-distance curve is calculated to verify the accuracy of the new curve.

Correction for the beam-walk effect

In a tip scanning AFM, the laser, used to detect the deflection of the cantilever, is attached on top of a hollow piezo tube, which has a small lens at the bottom to focus the laser on the cantilever. A schematic drawing of the PicoSPM LE, a tip scanning AFM, is shown in fig. 3.4a. During a force-distance curve the distance

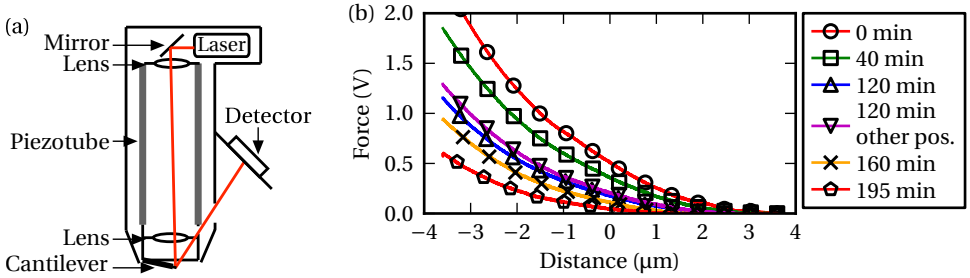

Figure 3.4:
(a) Schematic drawing of the PicoSPM LE, a tip scanning AFM. During a force-distance curve, the lens changes position, changing the deflection signal.
(b) Contact free force-distance curves made in liquid. Curves were measured at a variety of x, y positions and over an extended length of time.

between the laser and the lens changes slightly, which changes the laser spot and makes the beam move over the cantilever. This “beam-walk” effects produces a slight artifact in the apparent cantilever deflection.

Additionally, since all the tissues are measured under aqueous conditions, differences in condensation on the lens and other optics of the AFM make the beam-walk effect change over time. These optical effects change the deflection signal, making it seem as if the cantilever is experiencing a force, while in fact it is still far above the surface. This effect is illustrated in fig. 3.4b.

Initially, the functional form of the "beam-walk" effect was measured by making force-distance curves in liquid about one hundred microns above the surface. We find that the change of the deflection signal as a function of the piezo height can well be approximated by a second order polynomial.

As the optical effect changes with time and tip position, the parameters for the background correction need to be measured for each curve separately. A quadratic fit is made over the first 33% of the force-distance curve. This criterium proved to provide sufficiently many datapoints to give a good estimate of the background, without having the risk of using data where the tip is already in contact with the surface. The estimate of the "beam-walk" effect is improved by performing a median average of each fit with the fits from the adjacent force-distance curves.

This method of correcting force-distance curves is demonstrated by making a force-volume measurement on a piece of cartilage from a pig knee joint. Two typical force-distance curves before and after the correction are shown in fig. 3.5. The fitting correction reduces the artifact of apparent deflection to less than 1nm. The measured stiffness before and after correction differs up to 30%.

This correction also removes the systematic error that makes raised areas of

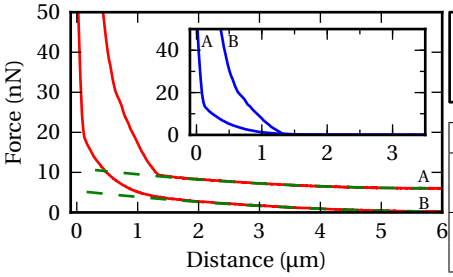

		Corrected	Uncorrected
A	Work	3.8 μm nN	6.2 μm nN
	Young's mod.	0.27 MPa	0.21 MPa
B	Work	2.1 μm nN	5.7 μm nN
	Young's mod.	0.36 MPa	0.22 MPa

Figure 3.5:
Corrected and uncorrected force-distance curves on pig cartilage. The "beam-walk" effect is measured by making a quadratic fit to the first 33% of the curve. Afterwards the fit is averaged with its adjacent fits and subtracted from the original force-distance curve. This reduces the artifact of apparent deflection to less than 1 nm and gives a correction to the measured stiffness in the order of 30%.

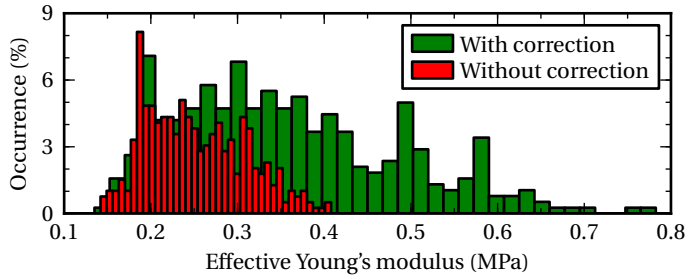

Figure 3.6:
Histogram of the measured stiffnesses on a piece of pig cartilage, before and after the background correction. The force-distance curves were made on a grid of 75 μm × 75 μm.

the sample appear stiffer than the lower areas. The lower areas of the tissue have a longer distance before the tip touches the sample. Since for the uncorrected curves the cantilever seems to be deflected before the point of contact, the total work done until the set force is reached seems to be higher. For rough samples, with height variations of several micrometers, this effect can dominate over the stiffness variations of the sample.

When all the force-distance curves made in one measurement are put together in one histogram, fig. 3.6, the significance of the correction is very clear. The optical artifact of the apparent deflection gives rise to an underestimation of the stiffness in the order of 30%. The fact that the magnitude of the error changes over time, makes the correction even more essential.

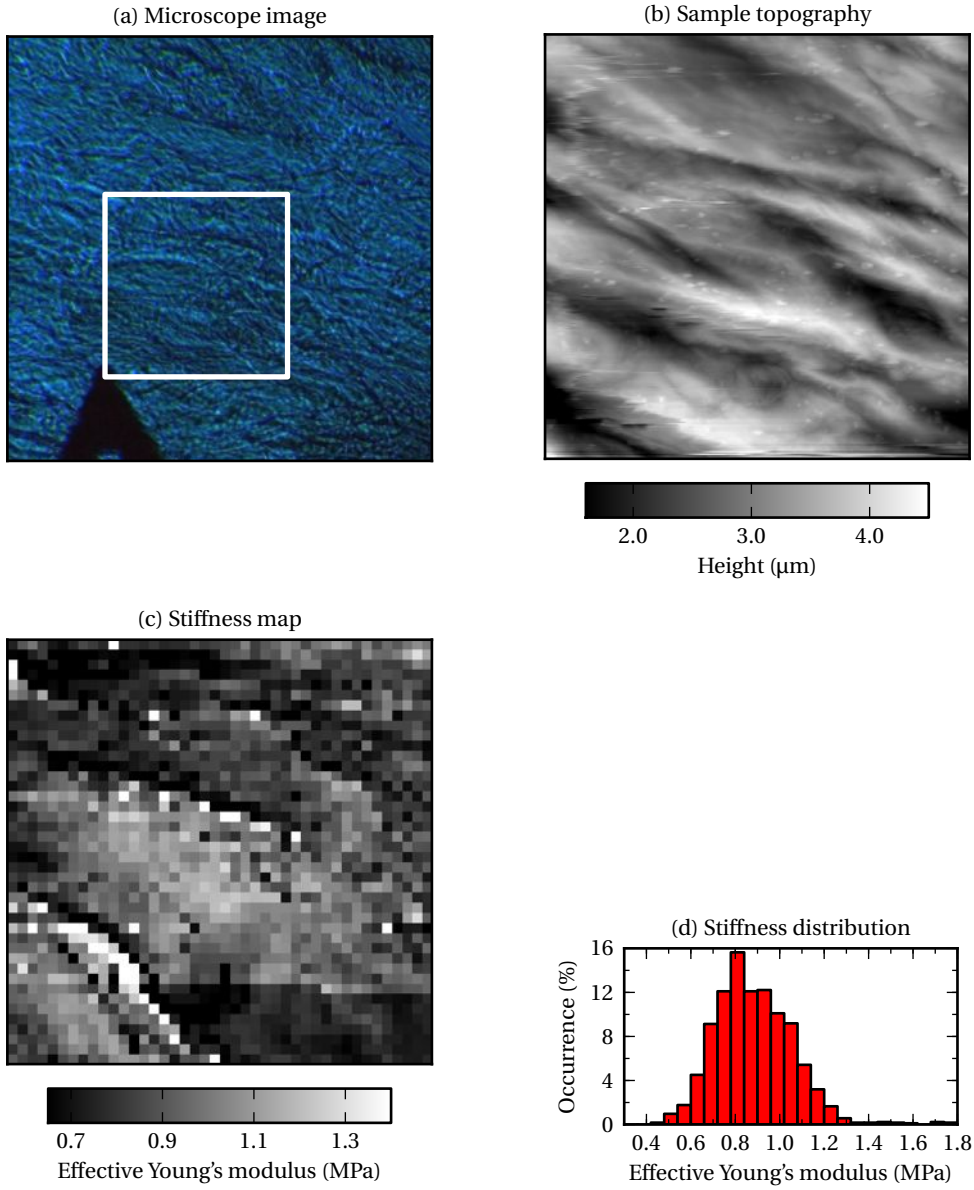

Figure 3.7:
Example measurement on a piece of porcine aortic wall. The inverted microscope is used to select the region (a) on which first the samples topography (b) is measured. The white square shows the area, 113 µm × 113 µm, which is being imaged with the AFM. Afterwards a force-volume measurement is made and the effective Young's modulus is calculated for every indentation (c). Stiffer, elongated, regions in the stiffness map tend to correlate with higher regions in the height image, which both have the same orientation as the fibers seen through the microscope. (d) Shows the distribution of the stiffnesses from the stiffness map (c).

3.1.4 Example dataset

The optical microscope is used to select the region to be measured, while two micrometer screws allow for a precise positioning of the sample in x and y. The microscope image clearly shows a network composed of different fibers. When the AFM is used to make a height image of the same region, as is shown in fig. 3.7b, the same fiber-like structure is measured. Afterwards, the tissue is indented on a regular grid of points and the effective Young's modulus is calculated for every indention, as is shown in fig. 3.7c. Stiffer regions in the stiffness map are elongated in the same direction as the fibers in the optical images and tend to correlate with higher regions in the height image, suggesting they might be collagen fibers. When all individual stiffness measurements are combined into a histogram, fig. 3.7d, the distribution of stiffnesses of the sample can be studied.

3.2 Fluorescence microscopy

In this study different forms of fluorescence microscopy are used to study the arrangement of fibers which make up the aortic wall and determine the mechanical properties of the tissue. In this type of microscopy the sample is illuminated with light of a specific wavelength which is being absorbed by the tissue and re-emitted at a longer wavelength. Most often this process takes place in fluorophores which are either attached to specific proteins, e.g. a Alexa488 anti-body, or are naturally present in the sample, e.g. elastin fibers have a high autofluorescence.

A special form of fluorescence microscopy is multi-photon microscopy in which multiple photons are absorbed after which one photon is emitted with the combined energy of the absorbed photons, as is illustrated in fig. 3.8b.

3.2.1 Confocal microscopy

In a conventional (wide-field) fluorescence microscope, the entire sample is evenly illuminated by a light source. All parts of the sample are excited at the same time and the resulting fluorescence, detected by the microscope's photodetector, includes a large unfocused background. In contrast, a confocal microscope uses point illumination together with a pinhole to eliminate out-of-focus signal, as is schematically illustrated in fig. 3.9a, and it thereby greatly increases the image's optical resolution, particularly in the z direction.

Tissues are made up of a complex three-dimensional network of fibers. By collecting a series of images with the focal plane at different heights, a three-dimensional view of this network can be constructed. 3D imaging of the tissue

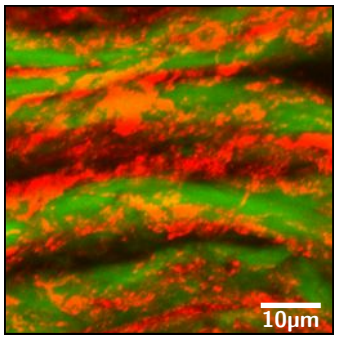

(a)

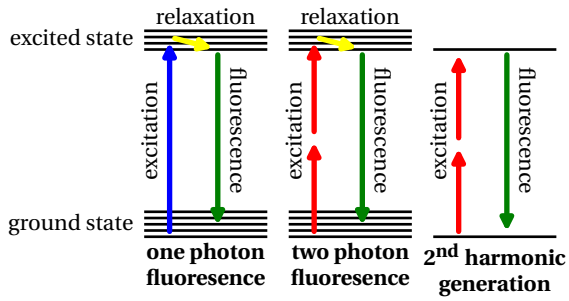

(b)

Figure 3.8:
(a) Fluorescence image of the aortic wall after it has been treated with enzymes which remove the proteoglycans, chapter 5. The collagen fibers (red) have been imaged using second-harmonic generation, while elastin (green) has been imaged using its two-photon autofluorescence.
(b) The basic principle of fluorescence microscopy. One or multiple photons are observed which bring an fluorphore into an excited state. When the fluorphore falls back to its ground state, it emits a photon.

not only gives a clear image of the organization of the different fibers, it also proved to be able to reveal structural changes in tissues which were hidden by conventional wide-field microscopy, fig. 3.9b,c.

In this study various different wide-field and confocal microscopes have been used. Tissues have been stained either chemically, e.g. with Pico Sirius Red, or with anti-bodies, to label different components of the vessel wall, e.g. collagen and hyaluron. Elastin has been imaged using its strong autofluorescence.

3.2.2 Multi-photon microscopy

Multi-photon microscopy is an imaging technique that relies on nonlinear light-matter interaction to provide high contrast and optical sectioning capabilities. The nonlinear signals which are responsible for forming the images are of two primary types: second-harmonic generation (SHG) and two-photon excited fluorescence (TPF).[38] Both types of nonlinear interactions occur naturally in biological tissues, enabling the imaging of tissues without the addition of exogenous contrast agents. Multi-photon microscopy has been widely used to image cells,[39, 40] tissues[41–44] and even unstained living specimens.[44–46]

In two-photon excited fluorescence (TPF), two photons of wavelength λ are absorbed to excite an electron to an excited state, fig. 3.8b.[47] Relaxation back to the ground state occurs through the emission of a photon having slightly less than the input energy (due to losses in the the transitions between the excited

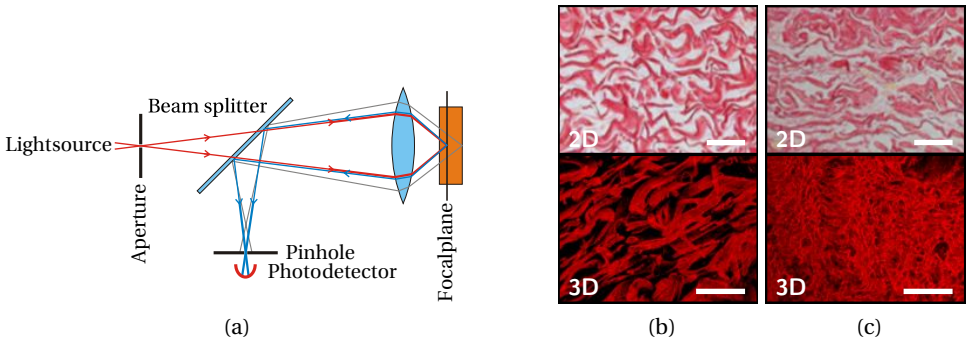

(a) (b) (c)

Figure 3.9:
(a) A confocal microscope uses a point illumination source together with a pinhole to eliminate the out-of-focus signal. This greatly increases the image's optical resolution, particularly in the z-direction.
(b), (c) Show a 2D and 3D image of the collagen structure of the adventitia of the abdominal aorta of a healthy individual (b) and a patient with Marfan syndrome (c). The 2D image is made with a bright field microscope, while the 3D image is a reconstruction made by projecting multiple optical sections taken by a confocal microscope. In the 3D image a clear difference in the network structure can be seen, while this remains largely hidden in the 2D image.
Scale bars: 30µm

states). This photon has a wavelength slightly greater than $\lambda/2$.

Second-harmonic generation, on the other hand, is primarily electronic in origin.[48] Two photons of the same wavelength "coalesce" to a virtual state within the specimen to form a single photon with an energy of exactly twice that of the incident photons, the emitted wavelength is $\lambda/2$. A detailed study on the electronic origin of this process shows that the intensity of the resulting signal strongly depends on the orientation, polarization and local symmetry properties of the molecule.[48]

Multi-photon microscopy has several advantages over one-photon confocal microscopy. The probability of two-photon absorption depends on the square of the intensity of the excitation light, and thereby only takes place in a very narrow volume at the focal point of the microscope. The maximum resolution is approximately 0.3µm in xy- and 0.9µm in z-direction, without the need of a pinhole.[49] Most tissues are transparent for near-infrared light, used in this type of microscopy, enhancing the depth penetration, eg. up to 250µm in rat aortas.[50] In addition, photobleaching and photodamage are drastically reduced.[49]

The chirality of the collagen molecule makes it a well known source of SHG, while the autofluorescence of elastin exhibits TPF.[41, 51] A study by Zoumi et al.[43] showed that both the collagen and the elastin can be excited at a wave-

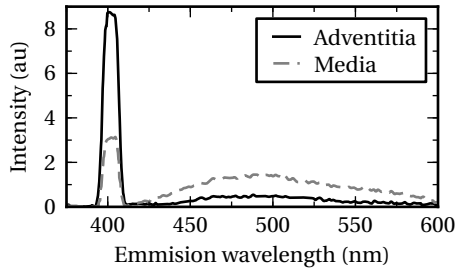

Figure 3.10:
Multi-photon emission spectra from a rabbit aortic wall excited at 800 nm showing the SHG peak of the collagen around 400 nm, and the broad TPF peak of elastin around 500 nm.[43]

length of 800 nm, fig. 3.10. By detecting the emitted light with a wavelength of 371 nm–425 nm for collagen and 471 nm–532 nm for elastin, both structures can be imaged simultaneously, fig. 3.8a. The multi-photon images were taken on a Zeiss 710 NLO upright confocal microscope equipped with a Spectra-Physics Deep See MP laser.

3.3 Sample preparation

All human arterial wall samples were provided by the Vascular Tissue Bank, Department of Vascular Surgery, Leiden, The Netherlands. Sample collection and handling was performed in accordance with the guidelines of Medical Ethical Committee of the Leiden University Medical Center and the code of conduct of the Dutch federation of Biomedical Scientific Societies.[52]

All aortic samples are cut to sections of approximately 1 cm thick, and are snap frozen within 24 hours after biopsy. Snap freezing is a method in which a small sample, a few mm^3, is quickly frozen by plunging it into liquid ethane (−183 °C). This freezing method prevents the formation of ice crystals which could damage the sample.

Afterwards the samples are cryosliced with a microtome (Leica CM3050S), and attached to Klinipath KP Plus microscope slides. Samples for AFM measurements and 2-photon imaging were cut to a thickness of 50 µm. This proved to be thick enough for the sample to remain intact in buffer for at least 24 hours. Samples used for (imuno)histochemistry were cut to a thickness of 5 µm, because thinner sections give less out of focus signal and chemical fixation would ensure that the sample remains intact. The samples are stored at −80 °C until use.

3.4 References

[1] G. Binnig and C. F. Quate. Atomic Force Microscope. *Phys. Rev. Lett.*, 56:930, 1986.

[2] G. Binnig and H. Rohrer. Scanning tunneling microscopy. *Surf. Sci.*, 126:236, 1983.

[3] F. Houze, R. Meyer, O. Schneegans, and L. Boyer. Imaging the local electrical properties of metal surfaces by atomic force microscopy with conducting probes. *Appl. Phys. Lett.*, 69:1975, 1996.

[4] S. N. Magonov, et al. Atomic force microscopy on polymers and polymer related compounds. *Polymer Bulletin*, 26:223, 1991.

[5] T. Thundat, D. P. Allison, R. J. Warmack, and T. L. Ferrell. Imaging Isolated Strands of Dna-Molecules by Atomic Force Microscopy. *Ultramicroscopy*, 42:1101, 1992.

[6] H. G. Hansma, et al. Reproducible imaging and dissection of plasmid DNA under liquid with the atomic force microscope. *Science*, 256:1180, 1992.

[7] P. Hallett, G. Offer, and M. J. Miles. Atomic force microscopy of the myosin molecule. *Biophys. J.*, 68:1604, 1995.

[8] Y. Lin, J. Wang, L.-J. Wan, and X.-H. Fang. Study of fibrinogen adsorption on self-assembled monolayers on Au(111) by atomic force microscopy. *Ultramicroscopy*, 105:129, 2005.

[9] M. Radmacher, et al. Imaging Adhesion Forces and Elasticity of Lysozyme Adsorbed on Mica with the Atomic-Force Microscope. *Langmuir*, 10:3809, 1994.

[10] M. Radmacher, R. W. Tillamnn, M. Fritz, and H. E. Gaub. From molecules to cells: imaging soft samples with the atomic force microscope. *Science*, 257:1900, 1992.

[11] H. Miyazaki and K. Hayashi. Atomic force microscopic measurement of the mechanical properties of intact endothelial cells in fresh arteries. *Med. Biol. Eng. Comp.*, 37:530, 1999.

[12] R. Resch, et al. Manipulation of gold nanoparticles in liquid environments using scanning force microscopy. *Ultramicroscopy*, 82:135, 2000.

[13] S. Park, K. D. Costa, and G. A. Ateshian. Microscale frictional response of bovine articular cartilage from atomic force microscopy. *J. Biomech.*, 37:1679, 2004.

[14] C. Stroh, et al. Single-molecule recognition imaging microscopy. *PNAS*, 101:12503, 2004.

[15] L. A. Chtcheglova, et al. Nano-Scale Dynamic Recognition Imaging on Vascular Endothelial Cells. *Biophys. J.*, 93:L11, 2007.

[16] C. L. Degen, et al. Nanoscale magnetic resonance imaging. *PNAS*, 106:1313, 2009.

[17] D. P. Allison, N. P. Mortensen, C. J. Sullivan, and M. J. Doktycz. Atomic force microscopy of biological samples. *Wiley Interdiscip Rev Nanomed Nanobiotechnol*, 2:618, 2010.

[18] C. Das, K. H. Sheik, P. D. Olmsted, and S. D. Connell. Nano-scale mechanical probing of supported lipid bilayers with atomic force microscopy. *arXiv*, physics.bio-ph, 2010.

[19] M. Salerno, S. Dante, N. Patra, and A. Diaspro. AFM Measurement of the Stiffness of Layers of Agarose Gel Patterned With Polylysine. *Microsc. Res. Techniq.*, 73:982, 2010.

[20] S. Kasas and G. Dietler. Probing nanomechanical properties from biomolecules to living cells. *Pflugers Arch.*, 456:13, 2008.

[21] M. M. J. F. Koenders, et al. Microscale mechanical properties of single elastic fibers: The role of fibrillin-microfibrils. *Biomaterials*, 30:2425, 2009.

[22] P. Grutter, D. Rugar, and H. J. Mamin. Magnetic force microscopy of magnetic materials. *Ultramicroscopy*, 47:393, 1992.

[23] A. Razatos, Y. L. Ong, M. M. Sharma, and G. Georgiou. Molecular determinants of bacterial adhesion monitored by atomic force microscopy. *PNAS*, 95:11059, 1998.

[24] C. Rotsch and M. Radmacher. Mapping local electrostatic forces with the atomic force microscope. *Langmuir*, 13:2825, 1997.

[25] G. Huber, S. N. Gorb, R. Spolenak, and E. Arzt. Resolving the nanoscale adhesion of individual gecko spatulae by atomic force microscopy. *Biol. Lett.*, 1:2, 2005.

[26] H. Hertz. Ueber die Berührung fester elastischer Körper. *Journal für die reine und angewandte Mathematik (Crelles Journal)*, 1882:156, 1882.

[27] I. N. Sneddon. The relation between load and penetration in the axisymmetric Boussinesq problem for a punch of arbitrary profile. *Int. J. Eng. Sci.*, 1965.

[28] E. A-Hassan, et al. Relative microelastic mapping of living cells by atomic force microscopy. *Biophys. J.*, 74:1564, 1998.

[29] J. H. N. Lindeman, et al. Distinct defects in collagen microarchitecture underlie vessel-wall failure in advanced abdominal aneurysms and aneurysms in Marfan syndrome. *PNAS*, 107:862, 2010.

[30] J. Sader, J. Pacifico, C. Green, and P. Mulvaney. General scaling law for stiffness measurement of small bodies with applications to the atomic force microscope. *J. Appl. Phys.*, 97:124903, 2005.

[31] H. J. Butt and M. Jaschke. Calculation of Thermal Noise in Atomic-Force Microscopy. *Nanotech.*, 6:1, 1995.

[32] R. Stark, T. Drobek, and W. Heckl. Thermomechanical noise of a free v-shaped cantilever for atomic-force microscopy. In *Ultramicroscopy*, 207–215 (Univ Munich, Inst Kristallog & Angew Mineral, D-80333 Munich, Germany, 2001).

[33] J. L. Hutter and J. Bechhoefer. Calibration of atomic-force microscope tips. *Rev. Sci. Instrum.*, 64:1868, 1993.

[34] H. Bueckle. Micro-Hardness Test and its Application. Berliner Union Verlag, Stuttgart, 1965.

[35] H. Bueckle. The science of hardness testing and its research applications. American Society for Metals, Ohio, 1973.

[36] I. K. Piechocka, A. S. G. van Oosten, R. G. M. Breuls, and G. H. Koenderink. Rheology of heterotypic collagen networks. *Biomacromolecules*, 12:2797, 2011.

[37] C. Storm, et al. Nonlinear elasticity in biological gels. *Nature*, 435:191, 2005.

[38] A. Zoumi, A. Yeh, and B. J. Tromberg. Imaging cells and extracellular matrix in vivo by using second-harmonic generation and two-photon excited fluorescence. *PNAS*, 99:11014, 2002.

[39] J. M. Squirrell, D. L. Wokosin, J. G. White, and B. D. Bavister. Long-term two-photon fluorescence imaging of mammalian embryos without compromising viability. *Nat. Biotechnol.*, 17:763, 1999.

[40] P. J. Campagnola, M. D. Wei, A. Lewis, and L. M. Loew. High-resolution nonlinear optical imaging of live cells by second harmonic generation. *Biophys. J.*, 77:3341, 1999.

[41] S. Roth and I. Freund. Optical second-harmonic scattering in rat-tail tendon. *Biopolymers*, 20:1271, 1981.

[42] T. Parasassi, et al. Two-photon microscopy of aorta fibers shows proteolysis induced by LDL hydroperoxides. *Free Radic. Biol. Med.*, 28:1589, 2000.

[43] A. Zoumi, X. Lu, G. Kassab, and B. Tromberg. Imaging coronary artery microstructure using second-harmonic and two-photon fluorescence microscopy. *Biophys. J.*, 87:2778, 2004.

[44] Y. Guo, et al. Second-harmonic tomography of tissues. *Opt. Lett.*, 22:1323, 1997.

[45] M. J. Levene, et al. In vivo multiphoton microscopy of deep brain tissue. *J. Neurophysiol.*, 91:1908, 2004.

[46] B. Masters, P. So, and E. Gratton. Multiphoton excitation fluorescence microscopy and spectroscopy of in vivo human skin. *Biophys. J.*, 72:2405, 1997.

[47] I. Freund, M. Deutsch, and A. Sprecher. Connective tissue polarity. Optical second-harmonic microscopy, crossed-beam summation, and small-angle scattering in rat-tail tendon. *Bio-*

phys. J., 50:693, 1986.

[48] R. Gauderon, P. B. Lukins, and C. J. Sheppard. Optimization of second-harmonic generation microscopy. *Micron*, 32:691, 2001.

[49] K. König. Multiphoton microscopy in life sciences. *J. Microsc*, 200:83, 2000.

[50] C. J. de Grauw, et al. Two-photon lifetime imaging of blood and blood vessels. *Proc. SPIE*, 4262:171, 2001.

[51] E. Georgiou, T. Theodossiou, and V. Hovhannisyan. Second and third optical harmonic generation in type I collagen, by nanosecond laser irradiation, over a broad spectral region. *Opt. Comm.*, 176:253, 2000.

[52] Code of conduct of the Dutch federation of Biomedical Scientific Societies, http://www.federa.org/?s=1&m=78&p=&v=4.